

# Ultra-Light Dark Matter Simulations and Stellar Dynamics: Tension in Dwarf Galaxies for $m < 5 \times 10^{-21}$ eV

Luca Teodori,<sup>1</sup> Andrea Caputo,<sup>2,3</sup> and Kfir Blum<sup>1</sup>

<sup>1</sup>*Department of Particle Physics and Astrophysics,  
Weizmann Institute of Science, Rehovot 7610001, Israel*

<sup>2</sup>*Department of Theoretical Physics, CERN, Esplanade des Particules 1, P.O. Box 1211, Geneva 23, Switzerland*

<sup>3</sup>*Dipartimento di Fisica, “Sapienza” Università di Roma & Sezione INFN Roma1, Piazzale Aldo Moro 5, 00185, Roma, Italy*

We present numerical simulations of dark matter and stellar dynamics in Ultra Light Dark Matter halos tailored to mimic dwarf galaxies. For dark matter particle mass  $m \approx 1 \times 10^{-22}$  eV, dynamical heating causes the half-light radius to over-shoot surface brightness data of the Fornax galaxy. For  $m \approx 1 \times 10^{-21}$  eV, soliton core formation leads to a velocity dispersion peak incompatible with kinematics data. Extending the analysis to the Carina and Leo II galaxies, the tension persists up to  $m \approx 5 \times 10^{-21}$  eV. A caveat in our analysis is the omission of stellar self-gravity. This would not change dynamics today, but could affect extrapolation back in time if the stellar body was more compact in the past.

*Introduction.* UltraLight Dark Matter (ULDM) is a well-motivated dark matter candidate [1–3], originally proposed to solve some small-scales shortcomings of the Cold Dark Matter (CDM) paradigm [4]. The relic abundance can be easily explained through the vacuum misalignment mechanism [1]. An appealing feature of this model is that it exhibits observable signatures without assuming any interaction between dark matter and the Standard Model beyond gravity.

On scales comparable to the de-Broglie wavelength of ULDM with particle mass  $m$  and velocity dispersion  $\sigma$ ,

$$\frac{\lambda_{\text{dB}}}{2\pi} \approx \frac{1}{m\sigma} \approx 2 \text{ kpc} \left( \frac{1 \times 10^{-22} \text{ eV}}{m} \right) \left( \frac{10 \text{ km s}^{-1}}{\sigma} \right), \quad (1)$$

the wave nature of ULDM is manifest. In cosmology, effective wave-mechanical pressure suppresses structure formation, leading to constraints from the Cosmic Microwave Background (CMB) anisotropies and galaxy clustering [5], as well as from the Lyman-alpha forest, disfavoring (roughly)  $m \lesssim 10^{-21}$  eV [6–9]. In galaxies, wave mechanics causes density interference patterns, and the formation of cored profiles (“solitons” in the literature) near the center of potential wells. These features are seen in simulations by many groups [10–22] and are theoretically understood to a large extent [23–30]. The fluctuating density field is expected to affect dynamical heating, friction, and relaxation of the stellar body [21, 31–38]. In the soliton region, quasinormal mode oscillations [10, 30] and soliton random walk [39] also contribute to heating<sup>1</sup>.

We thus have two main differences of ULDM with respect to CDM, as far as galaxy dynamics is concerned: a cored profile on scales of  $\lambda_{\text{dB}}$  in contrast with a cusp [47], and dynamical heating from the soliton and the interference patterns. Given these features, it is important to understand whether ULDM halos are compatible

with observations. Analyses of rotationally-supported low-surface-brightness galaxies led to the bound  $m \gtrsim 1 \times 10^{-21}$  eV [48–50] (see also [51]). These analyses, however, focused on the soliton signature alone, and relied on ULDM-only simulation results from Refs. [11, 12] without self-consistent treatment of stellar dynamics. Ref. [11] itself (see also [52–55]) focused on dispersion-dominated dwarf galaxies, but they, too, did not simulate both the ULDM and the stars.

Here we focus on dispersion-dominated dwarfs, and perform numerical simulations that include both the ULDM and the stars, the latter treated as test particles. We explore different initial conditions and ULDM particle masses in the range  $1 \times 10^{-22} \text{ eV} \leq m/\text{eV} \leq 5 \times 10^{-21} \text{ eV}$ . Our simulations are tailored to resemble the Fornax dwarf galaxy, and we compare our results with available data [56, 57].

The ULDM density profile in our simulations is initialized without a soliton core, but forms it dynamically to a level roughly consistent with the soliton-halo relation discovered in Ref. [12]. We show that the stellar line-of-sight velocity dispersion (LOSVD) profile approximately follows the steady solution to the collisionless Jeans’ equation. However, dynamical heating leads to secular growth of the stellar half-light radius, with a time scale that decreases with increasing  $m$ , qualitatively consistent with analytical expectations [27, 28]. Together, these effects put ULDM in tension with Fornax data for  $m \lesssim 1 \times 10^{-21}$  eV. In particular, for  $m = 1 \times 10^{-22}$  eV, the stellar body is contained inside the soliton region and LOSVD can in principle be reconciled with data; however, the dynamical heating timescale is much smaller than the system age of order 10 Gyr. This makes the half-light radius observed today difficult to explain without fine-tuning the initial conditions. For  $m = 1 \times 10^{-21}$  eV, dynamical heating becomes less important; however, the soliton occupies only the inner part of the stellar body, causing a bump in LOSVD, in tension with the data.

The scaling properties of the Schrödinger-Poisson

<sup>1</sup> Additional purely gravitational probes of ULDM include [40–46].

equation (SPE), that governs ULDM dynamics [1], relate our results derived for Fornax to results corresponding to larger  $m$  in halos with smaller velocity dispersion and smaller scale size, like Leo II and Carina dwarf galaxies, see Supplemental Material (SM) B. We perform simulations for these systems and find that the ULDM model tension with data extends up to  $m \approx 5 \times 10^{-21}$  eV.

This paper is structured as follows. We first summarize the simulations and describe the relevant output quantities. Next, we compare the simulation results with observational data. We then discuss the constraints derived from our simulations and compare them with previous works. We conclude with remarks on caveats and future directions.

*Simulations.* We simulate halos resembling the Fornax, Leo II, and Carina dwarf galaxies. For Fornax we use  $M_{200} \approx 10^9 M_\odot$ , in a box of length  $L = 40$  kpc ( $L = 12$  kpc) for  $m = 1 \times 10^{-22}$  eV ( $m \gtrsim 1 \times 10^{-21}$  eV) respectively. For Carina/Leo II,  $M_{200} \approx 10^8 M_\odot$ , in a box of length  $L = 5$  kpc for  $m = 5 \times 10^{-21}$  eV. We initialize the ULDM field to a halo with either a cusp NFW [47] or a cored Burkert [60] profile, and the stars to a Plummer profile [61, 62], using a version of the Edgington procedure described in the SM A. The ULDM field, together with the stars, are then evolved numerically for about 10 Gyr, the typical age of the stellar population [63–65]. The ULDM is evolved using a pseudo-spectral SPE solver, whereas stars are evolved via a second-order leap-frog algorithm.

We run a suite of simulations, varying the initial conditions of the halo and the stellar distribution, in an attempt to make the stellar LOSVD and surface brightness in the simulation as close as possible to observations.

Additional details of the simulations can be found in SM A and SM B.

We initialize  $10^4$  stars in all our simulations. The stars are treated as test particles, and their gravitational potential is neglected. This approximation is a caveat that we discuss further below (see also SM C).

*Results.* We compare the results of our simulations with observational data of Fornax [57], Leo II and Carina galaxies [66], which we describe in SM D. Fig. 1 shows an example of simulation results and comparison with data, for Fornax. The left panel shows the stellar LOSVD in the simulation at time zero (red points) and after  $t \approx 9.9$  Gyr (blue points), compared with data (purple). The black line shows the prediction of a Jeans analysis using as input the true ULDM radially-averaged halo mass profile  $M(r)$ , stellar density  $\rho_*(r)$ , column density  $\Sigma_*(r_{\text{proj}})$ , and anisotropy parameter  $\beta(r)$  from the simulation. The right panel shows the stellar half-light radius, which exhibits secular growth. We also show the central soliton core size, which evolves to become more massive and more compact, consistent with the relation  $M_{\text{sol}} \propto 1/r_{\text{sol}}$  [1].

We conducted a suite of 38 simulations, varying the

DM mass, density profile type (NFW or Burkert) and scale radius, the initial stellar half-light radius, and the initial stellar velocity anisotropy parameter  $\beta$ . We now summarize the results of this survey.

For  $m = 1 \times 10^{-21}$  eV (example in Fig. 1), the LOSVD peak in the soliton region, along with the flat tail outside the soliton region, are difficult to reconcile with the data. A solution that fits the tail, overshoots the data in the inner region, and vice-versa. One might think that a negative anisotropy  $\beta$  parameter could help in lowering the inner LOSVD peak; however, ULDM heating injects radial anisotropy in the star distribution. In SM A, Fig. 4 shows an example of a simulation initialized with negative  $\beta = -0.3$ . As can be seen, during the simulation  $\beta$  quickly evolves towards positive values, and its final configuration resembles that of a simulation with zero initial  $\beta$ . This suggests that positive  $\beta$  is an attractor for stars in an ULDM halo (see also [38]), in agreement with the intuition that stars are “kicked out” from the center of the system into eccentric orbits.

Although the stellar distribution is not stationary, due to the ULDM dynamical heating, a stationary Jeans analysis continues to describe the system fairly well.

This result can be understood by comparing the heating timescale, derived in the idealized case of homogeneous isotropic ULDM background [27, 28]<sup>2</sup>

$$T_{\text{heat}} = \frac{3\sigma^6 m^3}{16\pi^2 G^2 \rho^2 \ln \Lambda} \approx 0.48 \text{ Gyr} \left( \frac{m}{1 \times 10^{-21} \text{ eV}} \right)^3 \times \left( \frac{\sigma}{10 \text{ km s}^{-1}} \right)^6 \left( \frac{0.01 M_\odot/\text{pc}^3}{\rho} \right)^2, \quad (2)$$

with the dynamical time of the system,

$$T_{\text{dyn}} = \frac{R}{v} \approx 0.1 \text{ Gyr} \left( \frac{R}{1 \text{ kpc}} \right) \left( \frac{10 \text{ km s}^{-1}}{v} \right), \quad (3)$$

which shows  $T_{\text{dyn}} \lesssim T_{\text{heat}}$  for  $m = 10^{-21}$  eV in a Fornax-like halo. Note, however, that our simulations are not homogeneous or isotropic, and naturally contain additional effects like soliton random walk [36, 67], so we expect Eq. (2) to be only qualitatively valid. In fact, we stress that we do not use Eq. 2 in any numerical computation, merely, here, to obtain a rough analytical understanding of the relevant time scale.

For  $m = 1 \times 10^{-22}$  eV (example in Fig. 2), the whole stellar body is inside the soliton region. It is then possible to find a soliton solution which fits the LOSVD and surface brightness data: this was a main result of Ref. [11]. However, this solution is a brief unstable transient. Because the heating timescale for this value of  $m$  is fast,

<sup>2</sup> We are grateful to H. Kim and J. Eby for early assessment of this point.

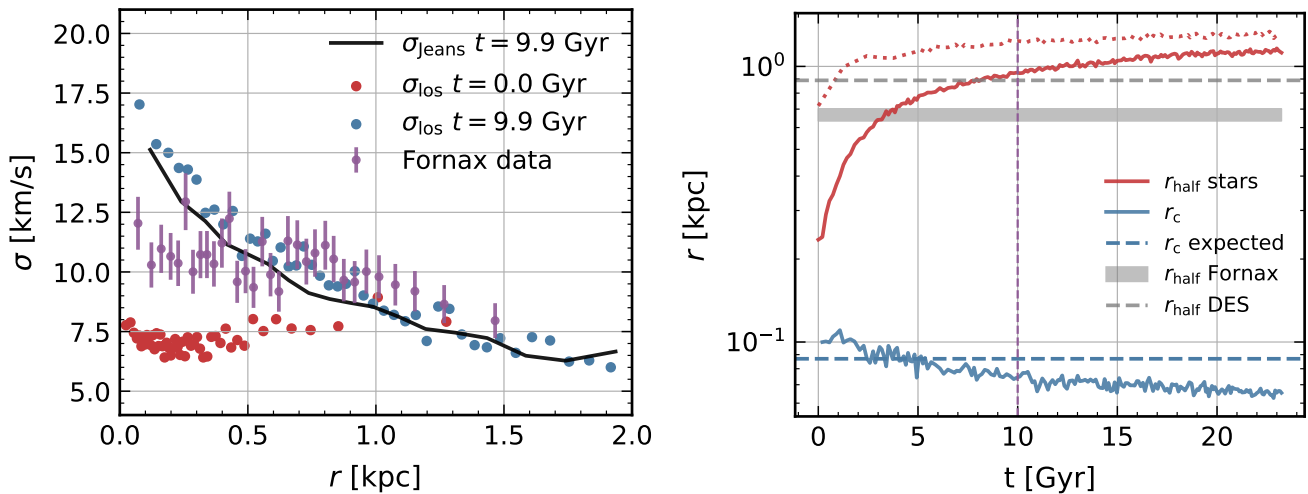


FIG. 1. Simulation results for  $m = 1 \times 10^{-21}$  eV, with  $L = 12$  kpc. **Left.** LOSVD data for Fornax (purple) is compared to the simulation at time 0 (red) and at time  $t \approx 9.9$  Gyr (blue). Every bin has the same number of stars. Black line is the  $\sigma_{\text{los}}$  predicted by a Jeans analysis. Notice that LOSVD data are difficult to reconcile with ULDM for  $r \lesssim 0.5$  kpc. **Right.** Red lines: half-light radius  $r_{\text{half}}$  evolution over time. Solid and dotted refer to two simulations, with the same ULDM halo but different initial distribution of stars. Grey band indicates the observed half-light radius of Fornax reported in Tab. I of Ref. [58],  $r_{\text{half}} = 0.668 \pm 0.034$  kpc, while grey dashed line shows the half-light radius from Ref. [59] (see discussion in SM D). Blue line shows the soliton core radius  $r_c$ . Dashed blue line shows the expectation from the soliton-halo relation of Ref. [12]. Vertical dashed line highlights  $t = 10$  Gyr, which is the typical age of the systems we consider. Notice that fine-tuned initial conditions allow to reproduce the half-light radius from [59] (albeit not from [58]).

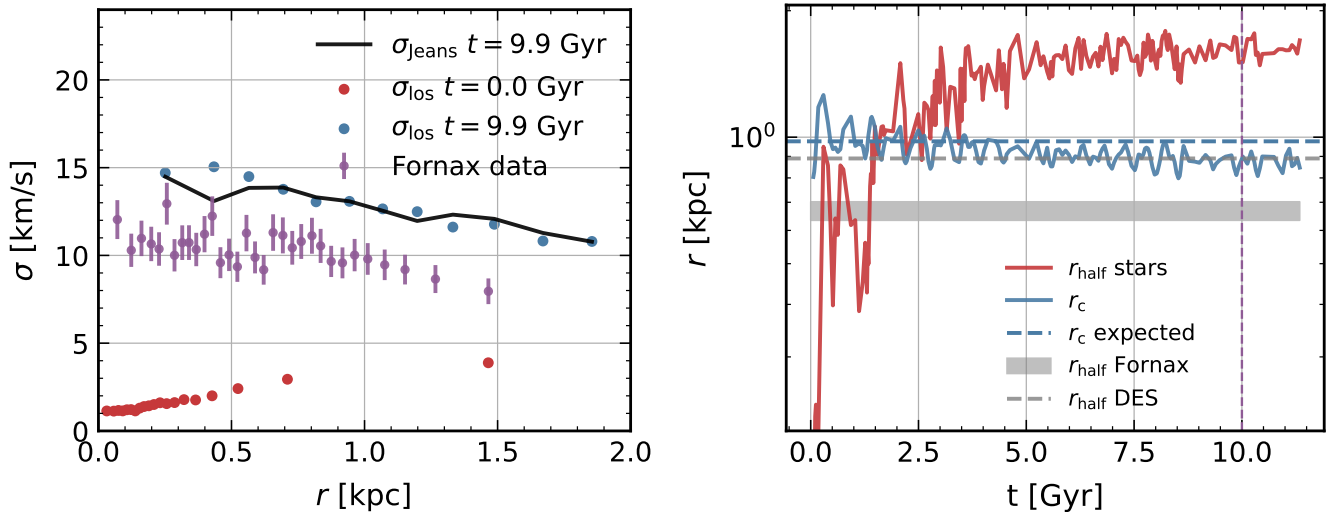


FIG. 2. Simulation for a Fornax-like system for  $m = 1 \times 10^{-22}$  eV, with  $L = 40$  kpc. Panels explanation is the same as in the caption of Fig. 1. The rapid increase of stellar  $r_{\text{half}}$  makes matching both stellar kinematics and surface brightness profile difficult, for a  $\sim 10$  Gyr old system.

the LOSVD grows with time and exceeds the observed range.

This increase can be traced to the rapid stellar half-light radius  $r_{\text{half}}$  growth, which also makes it difficult to justify the half-light radius seen in the data today. (See, however, the discussion of our neglect of stellar self-gravity, expanded in SM C: this is not a major effect for stellar radius observed today, but can become important

if the stellar profile was much more compact in the past.)

For  $m > 1 \times 10^{-21}$  eV, the timescale for the formation of the soliton in a galaxy like Fornax exceeds 10 Gyr, reducing the soliton mass today and its impact on stellar LOSVD. Fig. 9 in SM E demonstrates this point with  $m = 5 \times 10^{-21}$  eV. We also find that for  $m \gtrsim 5 \times 10^{-21}$  eV dynamical heating is negligible. An adequate fit of the observational data of Fornax can be obtained in this case;

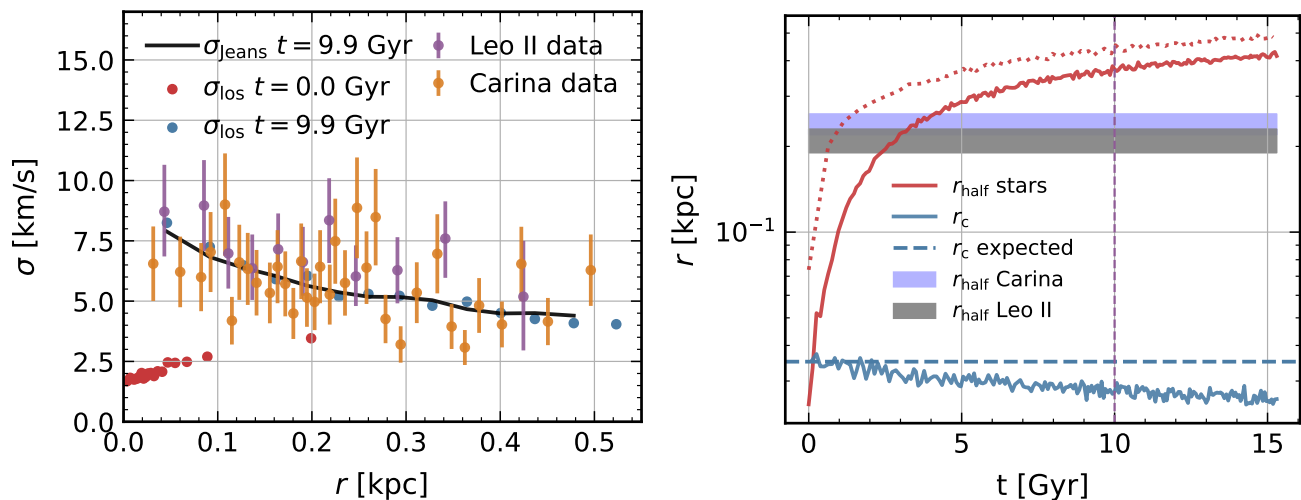


FIG. 3. Simulation of a halo resembling Leo II and Carina, with  $m = 5 \times 10^{-21}$  eV,  $L = 5$  kpc. Legend as in Fig. 1. Note the tension between simulated stellar  $r_{\text{half}}$  and data. For Leo II we derived LOSVD and  $r_{\text{half}}$  from Ref. [66], finding  $r_{\text{half}} = 0.21 \pm 0.02$  kpc with uncertainty determined via bootstrap resampling. For Carina we use data from Ref. [57]; in this case  $r_{\text{half}} = 0.24 \pm 0.02$  kpc.

this would be, in effect, simply a CDM-like model.

Considering also Leo II and Carina, we show a sample result of our simulations in Fig. 3, for  $m = 5 \times 10^{-21}$  eV. Contrary (and complementary) to Fig. 1 we see that in this case the LOSVD data can be reproduced rather well. However, the smaller velocities in these systems make dynamical heating faster, causing rapid growth of  $r_{\text{half}}$  that is difficult to reconcile with the observed value. We conclude that  $m \leq 5 \times 10^{-21}$  eV is in tension with data.

*Comparison with previous works.* We find it useful to compare our analysis with related works. Our bound  $m \geq 5 \times 10^{-21}$  eV is somewhat stronger than that found in [48–50] from disk galaxies. We note that while we did not explore  $m < 1 \times 10^{-22}$  eV, complimentary bounds from cosmology disfavor that regime [5–9].

Ref. [38] conducted similar (somewhat higher resolution) simulations of test-particle stars in an ULDM dwarf galaxy halo. Their results confirm ULDM-induced dynamical heating, leading to an increase of both the half-light radius and the  $\beta$  parameter of the stellar system. However, Ref. [38] considered only a single mass,  $m = 8 \times 10^{-23}$  eV, and did not report a comparison with observational data. In contrast, we explored a range of  $m$  and compared our results to data.

Ref. [68] used Leo II data to perform a Jeans analysis, varying the ULDM density profile and carefully comparing the results with data from [69]. They deduced the bound  $m \gtrsim 2.2 \times 10^{-21}$  eV, similar to the bound we inferred. However, the work was not based on ULDM simulations but rather on a parametric eigenstate expansion of the ULDM wave function. Consequently, Ref. [68] did not provide information about secular evolution, which our study suggests to be a significant effect of ULDM in

this mass range.

Finally, Ref.[35] (see also Ref.[21], and the related discussion in [22]) argued for the exclusion of  $m \lesssim 3 \times 10^{-19}$  eV, based on dynamical heating estimates and noting the stellar scale sizes and LOSVD in Segue 1 and Segue 2, but without self-consistent numerical simulations of the ULDM+stellar system. Our work here, based on simulations and applied to a different set of galaxies, is consistent with the conclusions of Ref. [35] in the range of  $m$  we simulated. (As an aside, the caveat in our analysis, due to omitting stellar self-gravity, applies also to Ref.[35], [21], and [22].)

*Conclusions and future directions.* DM-dominated dwarf galaxies can be used to study possible deviations from the CDM paradigm. In this work, we focused on how stellar kinematics and surface brightness data of dwarf spheroidal galaxies, in particular Fornax, Carina and Leo II, compare with an ULDM universe.

For  $m = 1 \times 10^{-21}$  eV, stellar velocity dispersion data from Fornax reveal a tension caused by the soliton core. At  $m = 1 \times 10^{-22}$  eV, a stationary Jeans analysis can fit the data, but dynamical heating renders this fit transient. The resulting stellar LOSVD and half-light radius evolve significantly, requiring fine-tuned initial conditions to match observations.

Galaxies with lower velocity dispersion and smaller scale radius are sensitive to higher values of  $m$ . We showed that for  $m = 5 \times 10^{-21}$  eV, the observed half-light radius of the Carina and Leo II dwarf galaxies is difficult to reconcile with the rapid ULDM heating-driven evolution, that tends to predict larger  $r_{\text{half}}$ . Our analysis suggests that Leo II and Carina (and other low-dispersion dwarfs) may allow to probe ULDM to larger values of  $m$ .

We postpone this study to future work.

We conclude with a word of caution regarding a caveat in our analysis. In our simulations, stars are treated as test particles. This leaves open the possibility, especially relevant if the stellar body was significantly more compact in the past, that stellar self-gravity and stellar feedback on the ULDM halo could mitigate the increase in  $r_{\text{half}}$ . In future work, we plan to incorporate  $N$ -body interactions and stellar feedback on the ULDM halo into our simulations.

*Acknowledgments.* We are grateful to J. Eby and H. Kim for their contributions to an early stage of this work. We thank J. Read for clarifications about the analysis in Ref. [68] and D. Blas for useful comments. We are grateful to E. Hardy and M. Gorghetto for useful discussion and guidance in the use of the pseudo-spectral solver, originally developed by E. Hardy. The authors acknowledge the support by the European Research Area (ERA) via the UNDARK project (project number 101159929). AC is also supported by an ERC STG grant (“Astro-DarkLS”, grant No. 101117510).

### Supplemental Material A: Eddington and Jeans analysis

We initialize halos via the Eddington procedure [33, 70]

$$f(x) = (\Delta v)^{3/2} \sum_{\vec{v}} \sqrt{f(x, \vec{v})} e^{im_i \vec{x} \cdot \vec{v} + i\varphi_{\vec{v}}}, \quad (\text{A1})$$

where  $\varphi_{\vec{v}}$  is a random phase dependent on  $\vec{v}$ ,  $\Delta v$  is the velocity spacing allowed by resolution in the simulation, and [71]

$$f(x, \vec{v}) = f_1(\mathcal{E}(x, v)) L^{-2\beta_0}, \quad L = xv \sin \eta, \quad (\text{A2})$$

where  $\beta_0$  is a constant anisotropy parameter,  $\eta$  is the angle between the  $\vec{x}$  and  $\vec{v}$  vector, and

$$\mathcal{E} = \Psi(r) - \frac{v^2}{2}, \quad \Psi = -\Phi + \Phi(r_{\text{max}}), \quad (\text{A3})$$

where  $\Phi$  is the gravitational potential. The value of  $r_{\text{max}}$  is chosen to be a few times the length of the simulation box.

If  $-0.5 < \beta_0 < 0.5$ , one can write [72]

$$f_1(\mathcal{E}) = \frac{2^{\beta_0 - \frac{3}{2}} \Gamma(\frac{3}{2} - \beta_0) \sin((\frac{1}{2} - \beta_0)\pi)}{\pi^{\frac{5}{2}} (\frac{1}{2} - \beta_0) \Gamma(1 - \beta_0)} \times \frac{d}{d\mathcal{E}} \int_0^{\sqrt{\mathcal{E}}} d\Psi \frac{d(r^{2\beta_0} \rho)}{d\Psi} (\mathcal{E} - \Psi)^{-\frac{1}{2} + \beta_0}; \quad (\text{A4})$$

In the case of  $\beta_0 = 0$ , Eq. (A4) reduces to

$$f_1(\mathcal{E}) = \frac{2}{\sqrt{8\pi^2}} \left( \frac{1}{2\sqrt{\mathcal{E}}} \frac{d\rho(\Psi=0)}{d\Psi} + \int_0^{\sqrt{\mathcal{E}}} dQ \frac{d^2\rho}{d\Psi^2}(Q) \right), \quad (\text{A5})$$

where  $Q = \sqrt{\mathcal{E} - \Psi}$ .

Stars are initialized using the same Eddington formalism, where  $\rho$  is the density profile of stars (e.g. Plummer) and  $\Phi$  is sourced by the dark matter halo. Once  $f^{\text{stars}}$  is computed, we can generate phase space coordinates for stars as follows. Choose a maximum radius  $R_{\text{max}}$  (typically, half the half length of the simulation box); then, the probability that a stars sits at a distance  $x$  is

$$p(x) = \frac{4\pi\rho(x)x^2}{M(R_{\text{max}})}, \quad (\text{A6})$$

and  $x$  coordinates are sampled using the cumulative of  $p(x)$ . The probability that a star has a velocity  $v$ , given its position  $x$ , reads

$$p(v|x) = \frac{p(v, x)}{p(x)} = \frac{f_1(\mathcal{E}(x, v))v^{2-2\beta_0}}{\int dv f_1(\mathcal{E}(x, v))v^{2-2\beta_0}}, \quad (\text{A7})$$

and again  $v$  coordinates are sampled via its cumulative. For the angle  $\eta$ , we use

$$p(\eta) = \frac{\sin^{1-2\beta_0} \eta}{\int d\eta \sin^{1-2\beta_0} \eta}. \quad (\text{A8})$$

The  $\theta, \phi$  angle for the  $\vec{x}$  spherical coordinates are sampled uniformly on the unit sphere; the components of the vector  $v$  in spherical coordinates then read

$$v_r = v \cos \eta, \quad v_\theta = v_r \cos \psi, \quad v_\phi = v_r \sin \psi, \quad (\text{A9})$$

where  $\psi$  is sampled uniformly on the unit circle. Then the Cartesian coordinates of  $\vec{v}$  are found via

$$\begin{pmatrix} v_x \\ v_y \\ v_z \end{pmatrix} = \begin{pmatrix} \sin \theta \cos \phi & \cos \theta \cos \phi & -\sin \phi \\ \sin \theta \sin \phi & \cos \theta \sin \phi & \cos \phi \\ \cos \theta & -\sin \theta & 0 \end{pmatrix} \begin{pmatrix} v_r \\ v_\theta \\ v_\phi \end{pmatrix}. \quad (\text{A10})$$

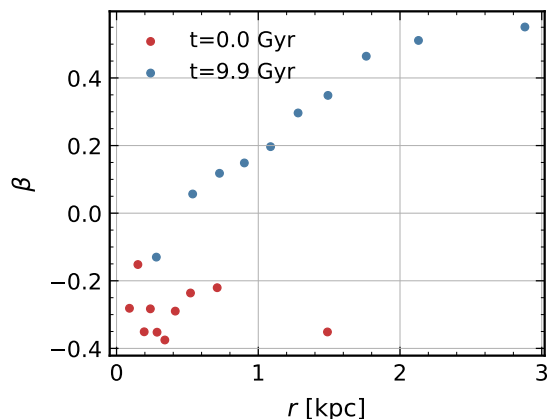


FIG. 4. Evolution of the anisotropy parameter for a simulation of a halo initialized as NFW, with  $L = 12$  kpc,  $m = 1 \times 10^{-21}$  eV, and initial  $\beta = -0.3$ . As noted in the main text,  $\beta$  evolves towards positive values due to ULDM dynamical heating.

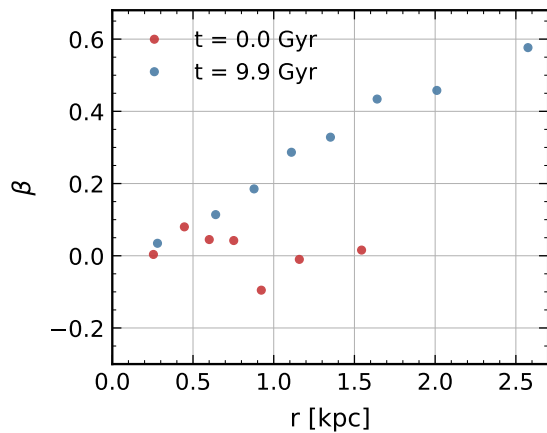


FIG. 5. Same as in Fig.4 but with initial  $\beta = 0$ .

We have the simulation data  $\vec{r}_i(t), \vec{v}_i(t)$  for the stars (labeled with the subscript  $i$ ), where  $\vec{r}$  is computed relative to the center of mass of the stars. Given a time  $t$  at which we want to compute velocity dispersions, we consider only the stars for which  $\max_{t' < t}(|\vec{r}_i(t')|) < R_{\max}$ , to avoid boundary artifacts. We then choose a random line of sight  $\hat{l}$ , we look for stars at a certain distance  $r_{\text{proj}}$ , where

$$r_{i,\text{proj}} = |\vec{r}_i - (\vec{r}_i \cdot \hat{l})\hat{l}|, \quad (\text{A11})$$

is the distance projected on the surface perpendicular to the random line of sight, and compute the variance of the projected velocity  $\vec{v}_i \cdot \hat{l}$  of all the stars falling into the shell of thickness  $dr_{\text{proj}}$ . This translates into

$$\sigma_{\text{los}}(r) = \sqrt{\text{Var}[\vec{v}(r) \cdot \hat{l}]}. \quad (\text{A12})$$

When comparing  $\sigma_{\text{los}}(r)$  with the result predicted by a spherically symmetric Jeans analysis, we numerically compute  $\rho_*(r)$ , the radially averaged star density,  $\Sigma_*(r_{\text{proj}})$ , the star column density along the line of sight  $\hat{l}$  radially averaged over the surface perpendicular to  $\hat{l}$ , and  $M(r)$ , the dark matter mass inside the radius  $r$ . We then use the radial velocity dispersion

$$\rho_*(r)\sigma_r^2(r) = G \int_r^{R_{\max}} ds \frac{\rho_*(s)M(s)}{s^2} e^{2 \int_r^s dz \beta(z)/z}, \quad (\text{A13})$$

where  $\beta(r)$  is the anisotropy parameter, defined as

$$\beta(r) = 1 - \frac{\sigma_\theta^2(r) + \sigma_\varphi^2(r)}{2\sigma_r^2(r)}, \quad (\text{A14})$$

where  $\sigma_\theta^2(r), \sigma_\varphi^2(r)$  are the tangential and azimuthal dispersion. Finally, the line of sight velocity dispersion reads

$$\begin{aligned} \sigma_{\text{los,Jeans}}^2(r_{\text{proj}}) &= \frac{2}{\Sigma_*(r_{\text{proj}})} \int_0^{\sqrt{R_{\max}^2 - r_{\text{proj}}^2}} dQ \\ &\times \left(1 - \beta \frac{r_{\text{proj}}^2}{Q^2 + r_{\text{proj}}^2}\right) (\rho_* v_r^2) (\sqrt{r_{\text{proj}}^2 + Q^2}). \end{aligned} \quad (\text{A15})$$

Our simulations show that  $\beta$  tends to become positive on a dynamical heating timescale. Figs. 4 and 5 show a sample halo initialized as an NFW with  $L = 12$  kpc and  $m = 1 \times 10^{-21}$  eV. In Fig. 4 we initialize  $\beta = -0.3$ , while for comparison, in Fig. 5 we initialize  $\beta = 0$ . As can be seen, both simulations evolve and reach similar values of  $\beta \approx +0.5$  by  $t \approx 10$  Gyr.

### Supplemental Material B: ULDM Simulation code

We employ a pseudo-spectral 3D Schrödinger-Poisson Equation (SPE) solver, which closely resembles the one described in [25]. Different versions of the same code, which do not include star dynamics, were used in [45, 73–75]. In the following, we review the basics of its implementations.

The SPE for the field  $\psi$  with mass  $m$  read (in our conventions,  $\psi$  has the dimensions of a mass squared, in particular the density is  $\rho = |\psi|^2$ )

$$i \frac{\partial \psi}{\partial t} = -\frac{1}{2m} \nabla^2 \psi + m \Phi \psi, \quad (\text{B1})$$

$$\nabla^2 \Phi = 4\pi G(|\psi|^2 - \langle |\tilde{\psi}|^2 \rangle). \quad (\text{B2})$$

It is possible to re-scale fields and coordinates in dimensionless variables. To this end, define

$$\tilde{\psi} = \frac{1}{\lambda^2} \sqrt{\frac{4\pi G}{m}} \psi, \quad \tilde{x} = \lambda m \vec{x}, \quad \tilde{t} = \lambda^2 m t, \quad \tilde{\Phi} = \Phi / \lambda^2, \quad (\text{B3})$$

with  $\lambda$  a dimensionless parameter. The mass  $M$ , energy  $E$ , and velocity  $v$  transform as follows

$$\tilde{M} = \frac{4\pi G m}{\lambda} M, \quad \tilde{E} = \frac{4\pi G m}{\lambda^3} E, \quad \tilde{v} = \frac{v}{\lambda}. \quad (\text{B4})$$

We can then recast Eq. (B1) as

$$i \frac{\partial \tilde{\psi}}{\partial \tilde{t}} = -\frac{1}{2} \nabla_{\tilde{x}}^2 \tilde{\psi} + \tilde{\Phi} \tilde{\psi}, \quad (\text{B5})$$

$$\nabla_{\tilde{x}}^2 \tilde{\Phi} = |\tilde{\psi}|^2 - \langle |\tilde{\psi}|^2 \rangle. \quad (\text{B6})$$

The energy associated to the field reads

$$\tilde{E}_{\text{tot}} = \tilde{E}_{\text{kin}} + \tilde{E}_{\text{pot}} = \int d^3 \tilde{x} \left( \frac{|\nabla \tilde{\psi}|^2}{2} + \frac{1}{2} |\tilde{\psi}|^2 \tilde{\Phi} \right). \quad (\text{B7})$$

Exploiting Eq. (B3), a simulation for ULDM particle mass  $m$ , total mass  $M$ , and typical velocity, length scale and time scale  $v, x, t$ , is equivalent to a simulation with  $m', M', v', x', t'$  via the correspondence

$$v' = \frac{1}{\lambda} v, \quad \frac{M'}{M} = \frac{x'}{x} = \frac{m}{\lambda m'}, \quad t' = \lambda^2 \frac{m}{m'} t, \quad (\text{B8})$$

with rescaling parameter  $\lambda$ . This feature can become useful for applying the results of one set of simulations

to physical galaxy systems of different characteristic mass and size.

The ULDM field is evolved via the unitary operator

$$\tilde{\psi}(\tilde{t} + d\tilde{t}) = \prod_{\alpha} e^{-id_{\alpha}d\tilde{t}\tilde{\Phi}_{\alpha}} e^{-ic_{\alpha}d\tilde{t}\frac{(-i\nabla)^2}{2}} \tilde{\psi}(\tilde{t}). \quad (\text{B9})$$

The equation is meant to be read from right to left, i.e. before one applies the kinetic operator

$$e^{-ic_{\alpha}d\tilde{t}\frac{(-i\nabla)^2}{2}} \tilde{\psi}(\tilde{t}) =: \tilde{\psi}^{(\alpha)}(\tilde{t} + d\tilde{t}), \quad (\text{B10})$$

and then the potential operator, where

$$\nabla^2 \tilde{\Phi}_{\alpha} = \sum |\tilde{\psi}^{(\alpha)}|^2. \quad (\text{B11})$$

The constants  $c_{\alpha}$ ,  $d_{\alpha}$  can be found in [25]. Eqs. (B10),(B11) are solved using fast Fourier transforms using the FFTW library [76].

We use adaptive time steps, to ensure a conservation of energy  $\Delta E/E \lesssim 10^{-5}$  between time-steps, and an overall conservation of energy  $|E_{\text{final}}^{\text{tot}} - E_{\text{initial}}^{\text{tot}}|/|E_{\text{final}}^{\text{tot}} + E_{\text{initial}}^{\text{tot}}| \lesssim 10^{-3}$ .

Star dynamics is computed from the gravitational potential  $\Phi$ , which is assumed to be sourced only from the ULDM field  $\psi$ , neglecting stellar gravity. Star coordinates are evolved via the leapfrog integrator [71]

$$\begin{aligned} \vec{r}_i(t_{j+1/2}) &= \vec{r}_i(t_j) + \frac{1}{2} dt \vec{v}_i(t_j), \\ \vec{v}_i(t_{j+1}) &= \vec{v}_i(t_j) - dt \nabla \Phi(\vec{r}_i(t_{j+1/2})); \\ \vec{r}_i(t_{j+1}) &= \vec{r}_i(t_{j+1/2}) + \frac{1}{2} dt \vec{v}_i(t_{j+1/2}). \end{aligned} \quad (\text{B12})$$

$\nabla \Phi(\vec{r}_i(t_{j+1/2}))$  is computed from the ULDM-sourced  $\Phi$  in the grid, using multi-linear interpolation. Stars coordinate initialization was described in Sec. A.

Our simulations generally exhibit soliton formation in good agreement with the original results of Ref. [12] (at least for  $m \lesssim 1 \times 10^{-21}$  eV, when the dynamical relaxation time is not too long, as noted in the text). Fig. 6 shows an example of ULDM density profile from a simulation initialized as an NFW halo with  $L = 40$  kpc,  $m = 1 \times 10^{-22}$  eV, evolved for 9.9 Gyr. The formation of a soliton core is clearly visible, with size consistent with expectations from the soliton-halo mass relation, and a functional form (blue curve fit) as predicted by Eq. 3 of Ref. [12].

### Supplemental Material C: When is stellar self-gravity important?

Our analysis, treating ULDM and stars dynamically in tandem and comparing the results directly to observational data, is a step forward in comparison to previous work. However, a remaining limitation is the treatment

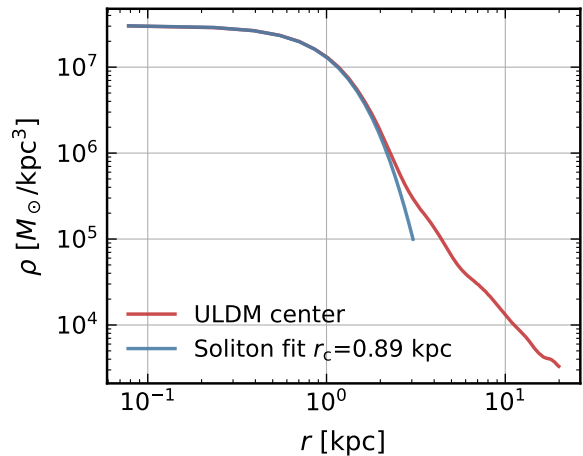


FIG. 6. ULDM density profile (red curve) for a simulation with  $L = 40$  kpc,  $m = 1 \times 10^{-22}$  eV, evolved for 10 Gyr. We also show (blue curve) the soliton fit using Eq. 3 of Ref. [12]; the resulting core radius is  $r_c = 0.89$  kpc, close to the value found in Ref. [12],  $r_{\text{expected}} = 0.98$  kpc.

of stars as test particles. This approximation seems reasonable given the dark-to-luminous mass ratios observed in dwarf spheroidal galaxies today, but it can fail if, in the past, the stellar population was more concentrated. For Fornax, Ref. [77] quotes a dark-to-luminous mass ratio of about 5–6 (16–18) within 1.6 (3) kpc [77]. To illustrate how the dark-to-luminous mass ratio scales with the parameters of interest and within the radius of the galaxy, let us assume an NFW profile for DM and a Plummer profile [61, 62] for the stellar distribution.

The enclosed NFW mass profile is given by

$$M_{\text{NFW}}(< r) = 4\pi r_s^3 \rho_s \left[ \ln\left(1 + \frac{r}{r_s}\right) - \frac{r}{r + r_s} \right], \quad (\text{C1})$$

while the enclosed Plummer profile is

$$M_{\text{Plummer}}(< r) = M_0^* \left( \frac{r}{r_{\text{half}}} \right)^3 \frac{1}{\left(1 + \frac{r}{r_{\text{half}}}\right)^{3/2}}, \quad (\text{C2})$$

where  $M_0^*$  is a normalization constant that accounts for the total number of stars, and  $r_{\text{half}}$  is their half-light radius.

In Fig. 7, we show the NFW mass profile (blue solid line) for  $r_s = 1.5$  kpc and  $\rho_s = 0.01 M_{\odot}/\text{pc}^3$ , which fits well the LOSVD data at large radii, alongside three different stellar mass profiles (black lines). The solid black curve corresponds to a Plummer profile with  $r_{\text{half}} = 0.7$  kpc, chosen to match the latest determination of Ref. [58] adopted in the main text, and a normalization  $M_0^*$  set so that

$$\frac{M_{\text{NFW}}(< 1.6 \text{ kpc})}{M_{\text{Plummer}}(< 1.6 \text{ kpc})} = 5. \quad (\text{C3})$$

In this case DM dominates by a factor of a few inside all the radii of interest. Then, the dashed and dotted

curves keep the same total stellar mass normalization (integrated to infinity) but reduce  $r_{\text{half}}$  to 0.4 kpc and 0.2 kpc, respectively.

We conclude that if the same number of stars were compressed by a factor  $\sim 3-4$  in their radial distribution, then stellar self-gravity would become significant, and eventually dominate the dynamics, rendering our simulations inadequate in that regime. This means that our simulations of the early evolution in some of the stellar half-light radius curves in Figs. 1, 2, and 3 are not fully consistent. The simulations should evolve into control once the stellar populations expand, within a few Gyr, and well before  $t \approx 10$  Gyr in all cases.

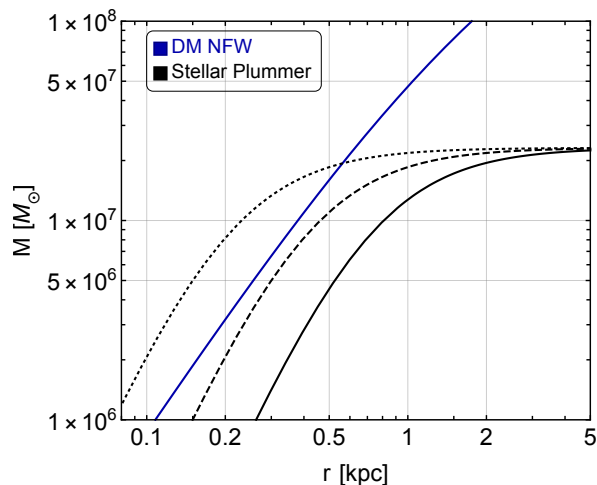


FIG. 7. NFW mass profile for DM with  $r_s = 1.5$  kpc and  $\rho_s = 0.01 M_\odot/\text{pc}^3$  (blue curve) and different stellar Plummer mass profiles (black curves). For the stellar profiles we have a Plummer profile with  $r_{\text{half}} = 0.7, 0.4, 0.2$  kpc, for the solid, dashed, and dotted curves, respectively.

#### Supplemental Material D: Dwarf galaxy data

For LOSVD data we have analyzed the following [repository](#) from Ref. [57]. This catalog has spectroscopic data for individual stars observed as part of the Michigan/MIKE Fiber System survey of four dwarf spheroidal galaxies: Carina, Fornax, Sculptor, and Sextans. For Fornax, following [57] we selected stars with membership probability of at least 95%. From these, we extracted stellar velocities, binned the data by radial distance from the galaxy center (ensuring each bin contained the same number of stars), and calculated the velocity dispersion for each bin.

We note that the choice of membership probability threshold can impact the results. Fig. 8 illustrates the LOSVD profiles for Fornax with two different membership probability thresholds: 95% (red data points) and 99% (blue data points). In both cases, each bin contains 60 stars. The results show that the stricter 99% thresh-

old substantially affects the inferred LOSVD profile. This cut also reduces the number of stars in the sample from 1920 to 1140.

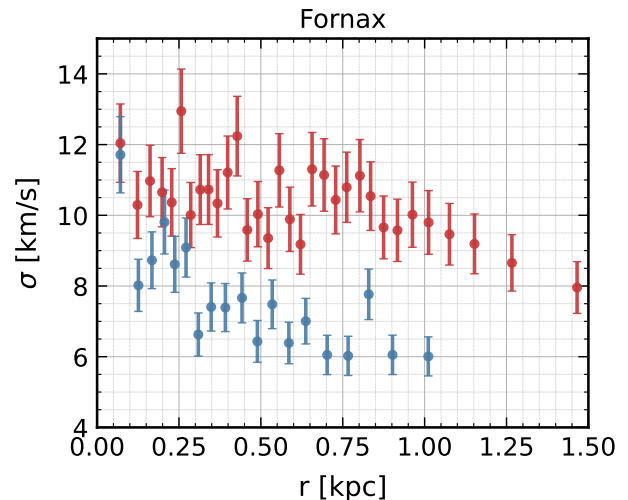


FIG. 8. LOSVD profile for Fornax. The red (blue) data points correspond to a 95% (99%) membership probability cut.

In the main text we quote the half-light radius reported in Tab. I of Ref. [58],  $r_{\text{half}} = 0.668 \pm 0.034$  kpc, which is also based on the data from the Michigan/MIKE Fiber System survey. (Ref. [58] has an Erratum which affects the half-light radius. See also the latest arXiv version of the paper.) The DES Collaboration [59] found a higher value from their survey  $r_{\text{half}} = 0.89$  kpc<sup>3</sup>, and we show that too in relevant plots for reference. It is worth noting that Table II of Ref. [59] shows that  $r_{\text{half}}$  can vary by a factor of two between, for example, the horizontal branch and the blue plume star sub-samples. The data for Carina was also obtained from Ref. [57] with membership probability cut of 95%. The half-light radius is  $r_{\text{half}} = 0.24 \pm 0.02$  kpc, where the uncertainty was determined via bootstrap resampling [79].

Finally, we have analyzed data for the Leo II dwarf spheroidal galaxy, available in this [repository](#). This dataset provides the LOSVD derived from 200 stars measured using the FLAMES/GIRAFFE spectrograph at the European Southern Observatory in Chile [66]. We applied the same cut as in Ref. [66], retaining only stars within  $3\sigma$  of the mean radial velocity. This cut reduced the number of stars to 171. These were then binned into groups of 12 stars each, reproducing fairly well Fig. 7 (left panel) from Ref. [66]. Using the same data we also derived the observed half light radius for this population to be  $r_{\text{half}} = 0.21 \pm 0.02$  kpc.

<sup>3</sup> Another study, based on older data [78], reports  $r_{\text{half}} = 0.710 \pm 0.077$  kpc (see their Table III).



**Supplemental Material E: Fornax simulation for  
 $m = 5 \times 10^{-21}$  eV and  $m = 10^{-22}$  eV**

In this section we present detailed results from two simulations of Fornax: one (Fig. 9) conducted with  $L = 8$  kpc,  $m = 5 \times 10^{-21}$  eV, and an initial  $\beta$  parameter set to zero in the Eddington procedure; and another (Fig. 10) with  $L = 40$  kpc,  $m = 1 \times 10^{-22}$  eV, and initial  $\beta \sim 0$ . These simulations represent the extremes of the  $m$  range we explored.

For the case of  $m = 5 \times 10^{-21}$  eV, ULDM heating is unimportant on the timescales of interest, and all quantities remain close to their initial values, including the stellar surface brightness profile, and the  $\beta$  parameter which fluctuates around zero. We checked that the spread in  $\beta$  around zero is consistent with random statistical fluctuations.

We also observe that the soliton core radius remains larger (by about a factor of 3) than would be expected from the naive soliton–halo relation. This suggests that dynamical relaxation is still ongoing in the system.

For the case of  $m = 1 \times 10^{-22}$  eV, the soliton encompasses the stellar body. The heating time-scale is much shorter in this case, and  $r_{\text{half}}$  doubles the observed one within  $\lesssim 4$  Gyr. We emphasize that even though a soliton can naively fit Fornax data according to a Jeans analysis, dynamical heating makes  $\sigma_{\text{los}}$  and  $r_{\text{half}}$  evolve in a nontrivial way. To illustrate this point, the bottom-right panel of Fig. 10 shows  $\sigma_{\text{los}}$  at an intermediate time  $t = 3$  Gyr through the simulation. Around that moment in time, both  $\sigma_{\text{los}}$  and  $r_{\text{half}}$  are roughly consistent with the data, compatible with the results of [11]. However, again, this is a short-lived transient state, and by  $t \approx 10$  Gyr both  $r_{\text{half}}$  and  $\sigma_{\text{los}}$  are off. Finally we note that the soliton in this case quickly relaxes close to the soliton–halo relation.

- 
- [1] L. Hui, J. P. Ostriker, S. Tremaine and E. Witten, *Ultralight scalars as cosmological dark matter*, *Phys. Rev. D* **95** (2017) 043541 [1610.08297].
- [2] L. Hui, *Wave Dark Matter*, *Ann. Rev. Astron. Astrophys.* **59** (2021) 247 [2101.11735].
- [3] E. G. M. Ferreira, *Ultra-light dark matter*, *Astron. Astrophys. Rev.* **29** (2021) 7 [2005.03254].
- [4] W. Hu, R. Barkana and A. Gruzinov, *Cold and fuzzy dark matter*, *Phys. Rev. Lett.* **85** (2000) 1158 [astro-ph/0003365].
- [5] A. Lagu e, J. R. Bond, R. Hlo ek, K. K. Rogers, D. J. E. Marsh and D. Grin, *Constraining ultralight axions with galaxy surveys*, *JCAP* **01** (2022) 049 [2104.07802].
- [6] V. Ir i c, M. Viel, M. G. Haehnelt, J. S. Bolton and G. D. Becker, *First constraints on fuzzy dark matter from Lyman-  forest data and hydrodynamical simulations*, *Phys. Rev. Lett.* **119** (2017) 031302 [1703.04683].
- [7] E. Armengaud, N. Palanque-Delabrouille, D. J. E. Marsh, J. Baur and C. Y eche, *Constraining the mass of light bosonic dark matter using SDSS Lyman-  forest*, *Mon. Not. Roy. Astron. Soc.* **471** (2017) 4606 [1703.09126].
- [8] T. Kobayashi, R. Murgia, A. De Simone, V. Ir i c and M. Viel, *Lyman-  constraints on ultralight scalar dark matter: Implications for the early and late universe*, *Phys. Rev. D* **96** (2017) 123514 [1708.00015].
- [9] K.-H. Leong, H.-Y. Schive, U.-H. Zhang and T. Chiueh, *Testing extreme-axion wave dark matter using the BOSS Lyman-Alpha forest data*, *Mon. Not. Roy. Astron. Soc.* **484** (2019) 4273 [1810.05930].
- [10] F. S. Guzman and L. A. Urena-Lopez, *Evolution of the Schrodinger-Newton system for a selfgravitating scalar field*, *Phys. Rev. D* **69** (2004) 124033 [gr-qc/0404014].
- [11] H.-Y. Schive, T. Chiueh and T. Broadhurst, *Cosmic Structure as the Quantum Interference of a Coherent Dark Wave*, *Nature Phys.* **10** (2014) 496 [1406.6586].
- [12] H.-Y. Schive, M.-H. Liao, T.-P. Woo, S.-K. Wong, T. Chiueh, T. Broadhurst and W. Y. P. Hwang, *Understanding the Core-Halo Relation of Quantum Wave Dark Matter from 3D Simulations*, *Phys. Rev. Lett.* **113** (2014) 261302 [1407.7762].
- [13] B. Schwabe, J. C. Niemeyer and J. F. Engels, *Simulations of solitonic core mergers in ultralight axion dark matter cosmologies*, *Phys. Rev. D* **94** (2016) 043513 [1606.05151].
- [14] J. Veltmaat and J. C. Niemeyer, *Cosmological particle-in-cell simulations with ultralight axion dark matter*, *Phys. Rev. D* **94** (2016) 123523 [1608.00802].
- [15] P. Mocz, M. Vogelsberger, V. H. Robles, J. Zavala, M. Boylan-Kolchin, A. Fialkov and L. Hernquist, *Galaxy formation with BECDM: I. Turbulence and relaxation of idealized haloes*, *Mon. Not. Roy. Astron. Soc.* **471** (2017) 4559 [1705.05845].
- [16] J. Veltmaat, J. C. Niemeyer and B. Schwabe, *Formation and structure of ultralight bosonic dark matter halos*, *Phys. Rev. D* **98** (2018) 043509 [1804.09647].
- [17] B. Eggemeier and J. C. Niemeyer, *Formation and mass growth of axion stars in axion miniclusters*, *Phys. Rev. D* **100** (2019) 063528 [1906.01348].
- [18] J. Chen, X. Du, E. W. Lentz, D. J. E. Marsh and J. C. Niemeyer, *New insights into the formation and growth of boson stars in dark matter halos*, *Phys. Rev. D* **104** (2021) 083022 [2011.01333].
- [19] B. Schwabe, M. Gosenca, C. Behrens, J. C. Niemeyer and R. Easther, *Simulating mixed fuzzy and cold dark matter*, *Phys. Rev. D* **102** (2020) 083518 [2007.08256].
- [20] J. Zhang, H. Liu and M.-C. Chu, *Cosmological Simulation for Fuzzy Dark Matter Model*, *Front. Astron. Space Sci.* **5** (2019) 48 [1809.09848].
- [21] D. J. E. Marsh and J. C. Niemeyer, *Strong Constraints on Fuzzy Dark Matter from Ultrafaint Dwarf Galaxy Eridanus II*, *Phys. Rev. Lett.* **123** (2019) 051103 [1810.08543].
- [22] B. T. Chiang, H.-Y. Schive and T. Chiueh, *Soliton Oscillations and Revised Constraints from Eridanus II of Fuzzy Dark Matter*, *Phys. Rev. D* **103** (2021) 103019 [2104.13359].
- [23] P.-H. Chavanis, *Mass-radius relation of Newtonian self-gravitating Bose-Einstein condensates with short-range interactions: I. Analytical results*, *Phys. Rev. D* **84** (2011) 043531 [1103.2050].

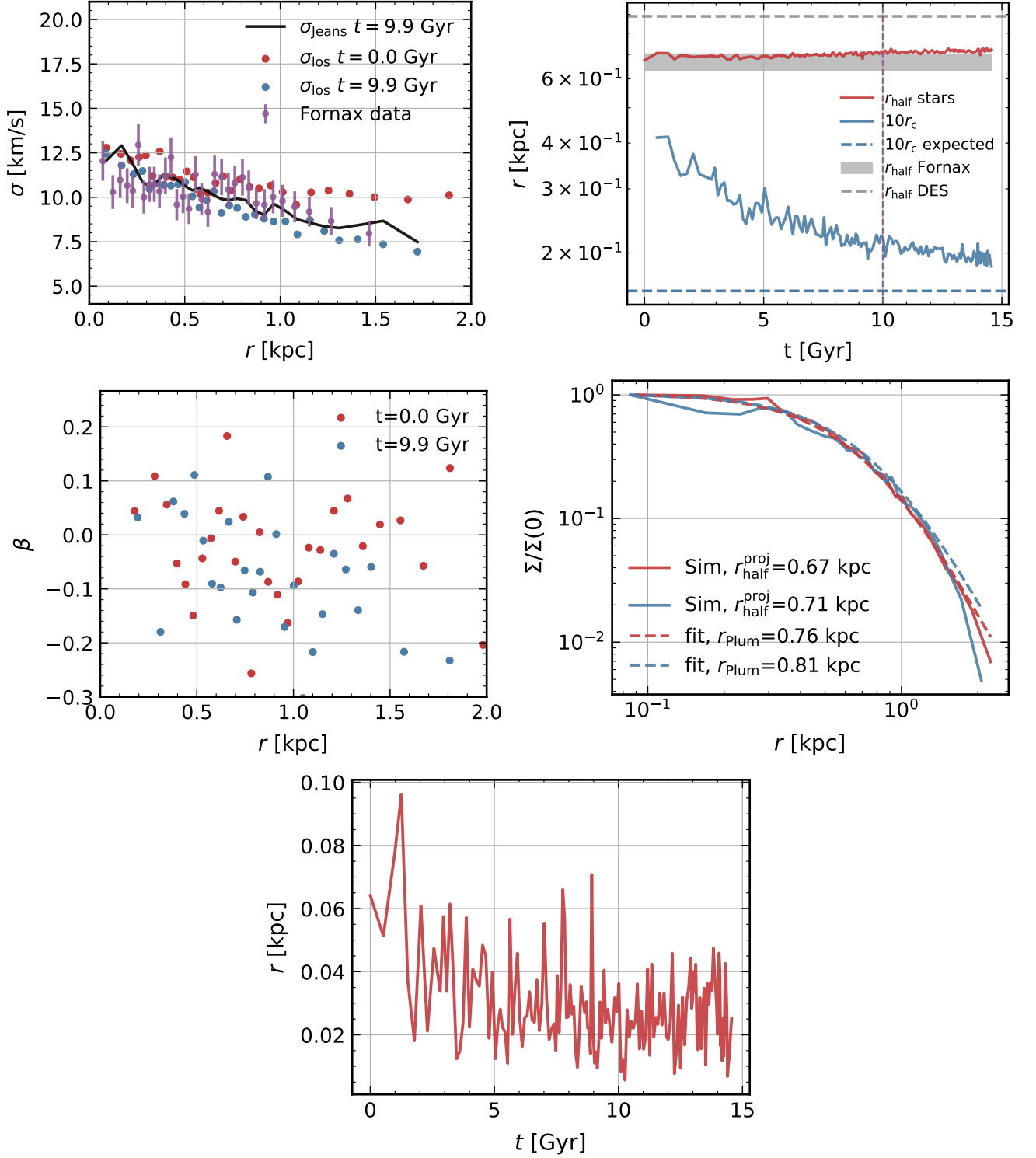


FIG. 9. Simulation initialized as an NFW halo, with  $L = 8$  kpc,  $m = 5 \times 10^{-21}$  eV. This is an example where dynamical heating is not significant, as we approach the “CDM limit” of ULDM. **Upper left.** LOSVD data for Fornax (purple) is compared to the simulation result at time 0 (red) and at time  $t \approx 9.9$  Gyr (blue). Black line is the  $\sigma_{\text{los}}$  predicted by a Jeans analysis. **Upper right.** Red line: stellar  $r_{\text{half}}$  evolution in time. Grey band shows the observed  $r_{\text{half}}$  from Ref. [58], grey dashed line shows  $r_{\text{half}}$  from Ref. [59]. Blue line shows the soliton core radius  $r_c$ . Dashed blue line shows the value of  $r_c$  expected from the soliton-halo relation of Ref. [12]. Vertical dashed line denotes  $t = 10$  Gyr. **Center left.** Anisotropy parameter  $\beta$  for  $t = 0$  (red) and  $t = 9.9$  Gyr (blue). **Center right.** Radially averaged stellar column density in the simulation for  $t = 0$  (red) and  $t = 9.9$  Gyr (blue), compared with a Plummer profile fit (dashed). We quote the Plummer scale parameter of the fit  $r_{\text{Plum}}$ , together with  $r_{\text{half}}^{\text{proj}}$  from the simulation. **Bottom.** Displacement between the stars center of mass and the maximum ULDM density point, which approximately coincides with the soliton.

- [24] P. H. Chavanis and L. Delfini, *Mass-radius relation of Newtonian self-gravitating Bose-Einstein condensates with short-range interactions: II. Numerical results*, *Phys. Rev. D* **84** (2011) 043532 [1103.2054].
- [25] D. G. Levkov, A. G. Panin and I. I. Tkachev, *Gravitational Bose-Einstein condensation in the kinetic regime*, *Phys. Rev. Lett.* **121** (2018) 151301 [1804.05857].
- [26] A. H. Guth, M. P. Hertzberg and C. Prescod-Weinstein, *Do Dark Matter Axions Form a Condensate with Long-Range Correlation?*, *Phys. Rev. D* **92** (2015) 103513 [1412.5930].
- [27] B. Bar-Or, J.-B. Fouvry and S. Tremaine, *Relaxation in a Fuzzy Dark Matter Halo*, *Astrophys. J.* **871** (2019) 28 [1809.07673].
- [28] B. Bar-Or, J.-B. Fouvry and S. Tremaine, *Relaxation in a Fuzzy Dark Matter Halo. II. Self-consistent Kinetic Equations*, *Astrophys. J.* **915** (2021) 27 [2010.10212].
- [29] J. H.-H. Chan, S. Sibiryakov and W. Xue, *Condensation and evaporation of boson stars*, *JHEP* **01** (2024) 071 [2207.04057].
- [30] J. H.-H. Chan, S. Sibiryakov and W. Xue, *Boson star normal modes*, *JHEP* **08** (2023) 045 [2304.13054].
- [31] N. C. Amorisco and A. Loeb, *First constraints on Fuzzy Dark Matter from the dynamics of stellar streams in the Milky Way*, **1808.00464**.
- [32] B. V. Church, J. P. Ostriker and P. Mocz, *Heating of Milky Way disc Stars by Dark Matter Fluctuations in Cold Dark Matter and Fuzzy Dark Matter Paradigms*, *Mon. Not. Roy. Astron. Soc.* **485** (2019) 2861 [1809.04744].
- [33] L. Lancaster, C. Giovanetti, P. Mocz, Y. Kahn, M. Lisanti and D. N. Spergel, *Dynamical Friction in a Fuzzy Dark Matter Universe*, *JCAP* **01** (2020) 001 [1909.06381].
- [34] N. Bar, D. Blas, K. Blum and H. Kim, *Assessing the Fornax globular cluster timing problem in different models of dark matter*, *Phys. Rev. D* **104** (2021) 043021 [2102.11522].
- [35] N. Dalal and A. Kravtsov, *Excluding fuzzy dark matter with sizes and stellar kinematics of ultrafaint dwarf galaxies*, *Phys. Rev. D* **106** (2022) 063517 [2203.05750].
- [36] H.-Y. Schive, T. Chiueh and T. Broadhurst, *Soliton Random Walk and the Cluster-Stripping Problem in Ultralight Dark Matter*, *Phys. Rev. Lett.* **124** (2020) 201301 [1912.09483].
- [37] H.-Y. Yang, B. T. Chiang, G.-M. Su, H.-Y. Schive, T. Chiueh and J. P. Ostriker, *Galactic disc heating by density granulation in fuzzy dark matter simulations*, *Mon. Not. Roy. Astron. Soc.* **530** (2024) 129 [2403.09845].
- [38] D. Dutta Chowdhury, F. C. van den Bosch, P. van Dokkum, V. H. Robles, H.-Y. Schive and T. Chiueh, *On the Dynamical Heating of Dwarf Galaxies in a Fuzzy Dark Matter Halo*, *Astrophys. J.* **949** (2023) 68 [2303.08846].
- [39] X. Li, L. Hui and T. D. Yavetz, *Oscillations and Random Walk of the Soliton Core in a Fuzzy Dark Matter Halo*, *Phys. Rev. D* **103** (2021) 023508 [2011.11416].
- [40] A. Khmel'nitsky and V. Rubakov, *Pulsar timing signal from ultralight scalar dark matter*, *JCAP* **1402** (2014) 019 [1309.5888].
- [41] K. Schutz, *Subhalo mass function and ultralight bosonic dark matter*, *Phys. Rev. D* **101** (2020) 123026 [2001.05503].
- [42] A. Laroche, D. Gilman, X. Li, J. Bovy and X. Du, *Quantum fluctuations masquerade as halos: Bounds on ultra-light dark matter from quadruply-imaged quasars*, **2206.11269**.
- [43] D. M. Powell, S. Vegetti, J. P. McKean, S. D. M. White, E. G. M. Ferreira, S. May and C. Spingola, *A lensed radio jet at milli-arcsecond resolution II: Constraints on fuzzy dark matter from an extended gravitational arc*, **2302.10941**.
- [44] K. Blum and L. Teodori, *Gravitational lensing  $H_0$  tension from ultralight axion galactic cores*, *Phys. Rev. D* **104** (2021) 123011 [2105.10873].
- [45] K. Blum and L. Teodori, *Axion  $H_0$  graphy: hunting for ultralight dark matter with cosmographic  $H_0$  bias*, **2409.04134**.
- [46] D. Blas, S. Gasparotto and R. Vicente, *Searching for ultra-light dark matter through frequency modulation of gravitational waves*, **2410.07330**.
- [47] J. F. Navarro, C. S. Frenk and S. D. M. White, *A Universal density profile from hierarchical clustering*, *Astrophys. J.* **490** (1997) 493 [astro-ph/9611107].
- [48] N. Bar, D. Blas, K. Blum and S. Sibiryakov, *Galactic rotation curves versus ultralight dark matter: Implications of the soliton-host halo relation*, *Phys. Rev. D* **98** (2018) 083027 [1805.00122].
- [49] N. Bar, K. Blum, J. Eby and R. Sato, *Ultralight dark matter in disk galaxies*, *Phys. Rev. D* **99** (2019) 103020 [1903.03402].
- [50] N. Bar, K. Blum and C. Sun, *Galactic rotation curves versus ultralight dark matter: A systematic comparison with SPARC data*, *Phys. Rev. D* **105** (2022) 083015 [2111.03070].
- [51] T. Bernal, L. M. Fernández-Hernández, T. Matos and M. A. Rodríguez-Meza, *Rotation curves of high-resolution lsb and sparc galaxies with fuzzy and multistate (ultralight boson) scalar field dark matter*, *Monthly Notices of the Royal Astronomical Society* **475** (2017) 1447–1468.
- [52] M. Safarzadeh and D. N. Spergel, *Ultra-light Dark Matter is Incompatible with the Milky Way's Dwarf Satellites*, **1906.11848**.
- [53] A. X. González-Morales, D. J. E. Marsh, J. Peñarrubia and L. A. Ureña López, *Unbiased constraints on ultralight axion mass from dwarf spheroidal galaxies*, *Mon. Not. Roy. Astron. Soc.* **472** (2017) 1346 [1609.05856].
- [54] H. Deng, M. P. Hertzberg, M. H. Namjoo and A. Masoumi, *Can Light Dark Matter Solve the Core-Cusp Problem?*, **1804.05921**.
- [55] V. Lora, J. Magana, A. Bernal, F. J. Sanchez-Salcedo and E. K. Grebel, *On the mass of ultra-light bosonic dark matter from galactic dynamics*, *JCAP* **02** (2012) 011 [1110.2684].
- [56] M. G. Walker, M. Mateo and E. Olszewski, *Stellar Velocities in the Carina, Fornax, Sculptor and Sextans dSph Galaxies: Data from the Magellan/MMFS Survey*, *Astron. J.* **137** (2009) 3100 [0811.0118].
- [57] M. G. Walker, M. Mateo, E. W. Olszewski, J. Penarrubia, N. W. Evans and G. Gilmore, *A Universal Mass Profile for Dwarf Spheroidal Galaxies*, *Astrophys. J.* **704** (2009) 1274 [0906.0341]. [Erratum: *Astrophys. J.* **710**, 886–890 (2010)].

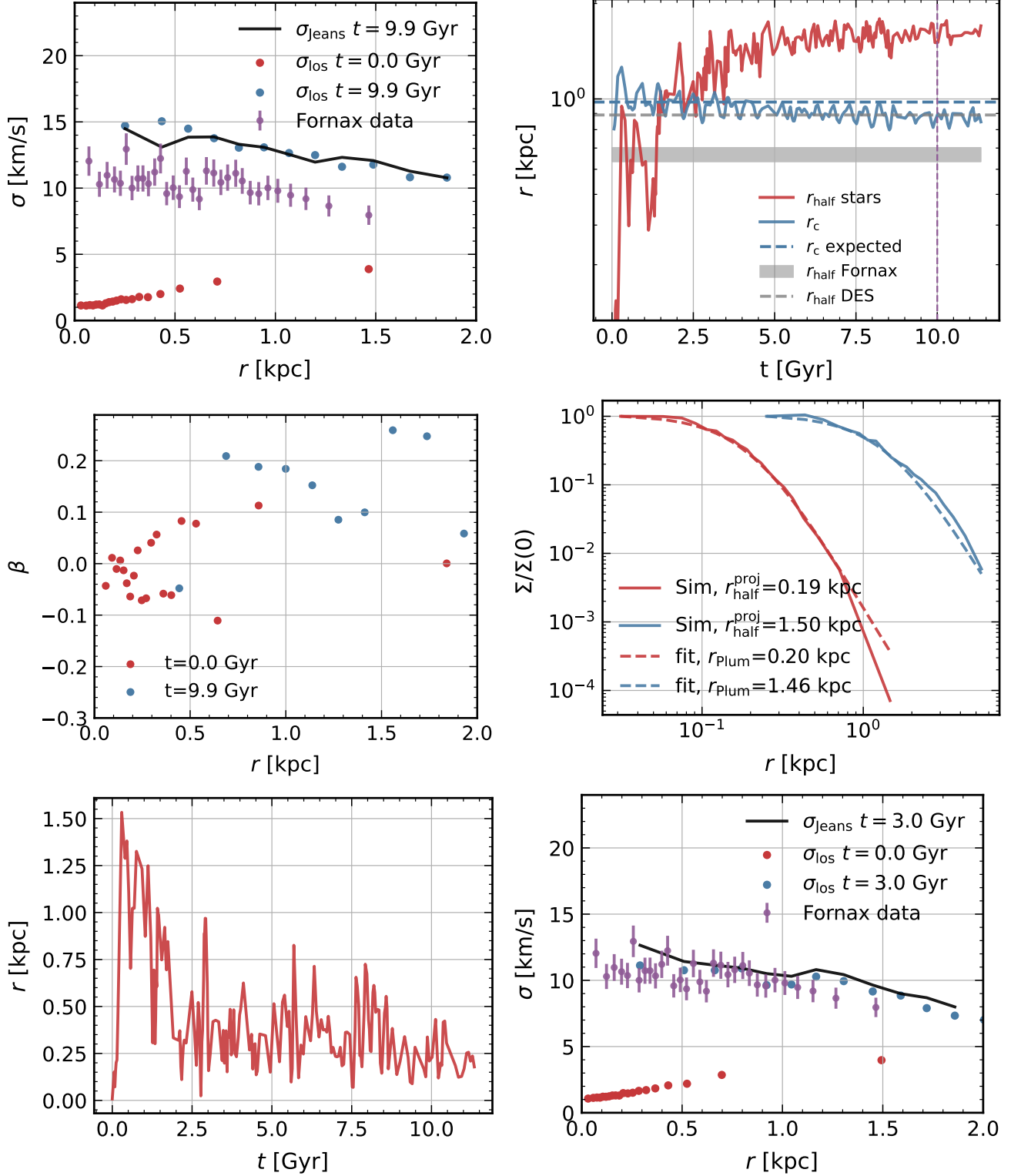


FIG. 10. Simulation for a Fornax-like system for  $m = 1 \times 10^{-22}$  eV, with  $L = 40$  kpc. Panels explanation is the same as in Fig. 9, with the addition of the bottom-right panel, which is the same as the upper-left panel, but for the  $t = 3$  Gyr snapshot.

- [58] M. G. Walker, M. Mateo, E. W. Olszewski, J. Peñarrubia, N. W. Evans and G. Gilmore, *A Universal Mass Profile for Dwarf Spheroidal Galaxies?*, *Astrophys. J.* **704** (2009) 1274 [0906.0341].
- [59] DES Collaboration, M. Y. Wang et al., *The morphology and structure of stellar populations in the Fornax dwarf spheroidal galaxy from Dark Energy Survey Data*, *Astrophys. J.* **881** (2019) 118 [1809.07801].
- [60] A. Burkert, *The Structure and Dark Halo Core Properties of Dwarf Spheroidal Galaxies*, *Astrophys. J.* **808** (2015) 158 [1501.06604].
- [61] H. C. Plummer, *On the problem of distribution in globular star clusters*, *MNRAS* **71** (1911) 460.
- [62] H. Dejonghe, *A completely analytical family of anisotropic Plummer models*, *MNRAS* **224** (1987) 13.
- [63] K. J. Mighell and R. M. Rich, *The leo ii dwarf spheroidal — an old galaxy with a large intermediate-age population*, *Astronomical Journal* **111** (1996) 777.
- [64] T. J. L. de Boer, E. Tolstoy, V. Hill, A. Saha, E. W. Olszewski, M. Mateo, E. Starkenburg, G. Battaglia and M. G. Walker, *The star formation and chemical evolution history of the fornax dwarf spheroidal galaxy*, *Astronomy & Astrophysics* **544** (2012) A73.
- [65] K. J. Mighell, *The carina dwarf spheroidal: an old galaxy with a large intermediate-age population*, *Astronomical Journal* **114** (1997) 1458.
- [66] A. Koch, J. T. Kleyna, M. I. Wilkinson, E. K. Grebel, G. F. Gilmore, N. W. Evans, R. F. G. Wyse and D. R. Harbeck, *Stellar kinematics in the remote Leo II dwarf spheroidal galaxy – Another brick in the wall*, *Astron. J.* **134** (2007) 566 [0704.3437].
- [67] D. Dutta Chowdhury, F. C. van den Bosch, V. H. Robles, P. van Dokkum, H.-Y. Schive, T. Chiueh and T. Broadhurst, *On the random motion of nuclear objects in a fuzzy dark matter halo*, *The Astrophysical Journal* **916** (2021) 27.
- [68] T. Zimmermann, J. Alvey, D. J. E. Marsh, M. Fairbairn and J. I. Read, *Dwarf galaxies imply dark matter is heavier than  $2.2 \times 10^{-21}$  eV*, 2405.20374.
- [69] M. E. Spencer, M. Mateo, M. G. Walker and E. W. Olszewski, *A multi-epoch kinematic study of the remote dwarf spheroidal galaxy leo ii\**, *The Astrophysical Journal* **836** (2017) 202.
- [70] L. M. Widrow and N. Kaiser, *Using the Schrodinger equation to simulate collisionless matter*, *Astrophys. J. Lett.* **416** (1993) L71.
- [71] J. Binney and S. Tremaine, *Galactic Dynamics: Second Edition*. 2008.
- [72] T. Lacroix, M. Stref and J. Lavalle, *Anatomy of Eddington-like inversion methods in the context of dark matter searches*, *JCAP* **09** (2018) 040 [1805.02403].
- [73] M. Gorghetto, E. Hardy, J. March-Russell, N. Song and S. M. West, *Dark photon stars: formation and role as dark matter substructure*, *JCAP* **08** (2022) 018 [2203.10100].
- [74] D. Budker, J. Eby, M. Gorghetto, M. Jiang and G. Perez, *A generic formation mechanism of ultralight dark matter solar halos*, *JCAP* **12** (2023) 021 [2306.12477].
- [75] M. Gorghetto, E. Hardy and G. Villadoro, *More axion stars from strings*, *JHEP* **08** (2024) 126 [2405.19389].
- [76] M. Frigo, *A fast fourier transform compiler*, *SIGPLAN Not.* **34** (1999) 169–180.
- [77] G. Battaglia, A. Sollima and C. Nipoti, *The effect of tides on the fornax dwarf spheroidal galaxy*, *Monthly Notices of the Royal Astronomical Society* **454** (2015) 2401–2415.
- [78] A. W. McConnachie, *The observed properties of dwarf galaxies in and around the local group*, *The Astronomical Journal* **144** (2012) 4.
- [79] B. Efron, *Bootstrap methods: Another look at the jackknife*, *The Annals of Statistics* **7** (1979) 1.